Electronic Supplementary Material (ESI) for Materials Horizons.
This journal is © The Royal Society of Chemistry 2021

SUPPLEMENTARY INFORMATION

The pursuit of stability *in halide perovskites*: the monovalent cation and *the key for surface and bulk self-healing*

D R Ceratti[1]***, *A V Cohen*[1], *R Tenne*[2], *Y Rakita*[1], *L Snarski*[1], *N P Jasta*[3,4], *L Cremonesi*[5], *R Cohen*[3], *M Weitman*[3] *I Goldian*[6], *I Kaplan-Ashiri*[6], *T Bendikov*[6], *V Kalchenko*[7], *M Elbaum*[8], *M A C Potenza*[5], *L Kronik*[1*], *G Hodes*[1*], *D Cahen*[1,3,4]***

[1]Weizmann Institute of Science, Department of Materials and Interfaces, 7610001, Rehovot, Israel.
[2]Weizmann Institute of Science, Department of Physics of Complex Systems, 7610001, Rehovot, Israel.
[3]Bar Ilan University, Department of Chemistry, 5290002, Ramat Gan, Israel
[4]Bar Ilan University, Bar-Ilan Institute for Adv. Mater., BINA, 5290002, Ramat Gan, Israel
[5]Department of Physics and CIMAINA, University of Milan, via Celoria, 16 20133, Milan, Italy.
[6]Weizmann Institute of Science, Department of Chemical Research Support, 7610001, Rehovot, Israel.
[7]Weizmann Institute of Science, Department of Veterinary Resources, 7610001, Rehovot, Israel.
[8]Weizmann Institute of Science, Department of Chemical and Biological Physics, 7610001, Rehovot, Israel.

*davide-raffaele.ceratti@weizmann.ac.il , david.cahen@weizmann.ac.il,
gary.hodes@weizmann.ac.il, leeor.kronik@weizmann.ac.il

In this file, we present the experimental details, calculations and discussions that could not be reported in the main text without making it tedious and excessively long. We report here the list of the titles of the section.

SI.1 Single Crystal Synthesis

$MAPbBr_3$, $FAPbBr_3$ and $CsPbBr_3$ single crystals were grown by the method reported in the supplementary information of ref. [1]. We add here details of the synthesis that help to obtain larger crystals with the anti-solvent method than before. To that end we cover the container with the perovskite precursors with filter paper. This avoids unwanted dropping of anti-solvent that condensed on the crystallization chamber walls. Any anti-solvent drop falling directly in the precursor solution induces the formation of multiple seeds, which reduces average crystal size.

The verification of the crystallinity of the single crystals was done as reported in the supplementary information of ref.[1].

SI.2. Two-photon (2P) vs one-photon (1P) microscopy

In 2P microscopy we can assess the bulk instead of the surface of a sample. Figure S1a illustrates how supra-bandgap laser light (488 nm- 8.0 µs dwell time)) is absorbed in the first layers of the halide perovskite single crystal due to the high value of the 1P absorption coefficient of the perovskite. 2P excitation is obtained using sub-bandgap light. To get sufficient intensity to yield a measurable, useful density of photons with twice the energy of the exciting ones at the focal point inside the crystal, we need to use a pulsed laser. We use excitation from a pulsed laser at 800 nm (9.97 µs dwell time), 1.55 eV, an energy well below the bandgap of the bromide halide perovskites, i.e., the single crystals are

transparent for these photons, which, thus, can penetrate the crystal. Because of the difference in refractive index between the air and the crystal, the focus of the microscope objective is distorted with consequent positive aberration. Despite this, the 800 nm light remains focused enough for 2P absorption, which happens where the laser intensity is most concentrated. We reported in ref. [1] the shape of the focus and intensity distribution of the laser in the 2P microscope both at the surface and in the bulk. In Figure S1 we show the shape of the 1P focus and laser light intensity distribution as used for this experiment. While the same objective serves the 2P and 1P experiments, the Gaussian profile of the 1P laser is narrower than the objective back entrance. The effective numerical aperture of the objective was determined to be NA=0.505 by mapping the power profile of the laser at different distances from the objective. This number was used as input to obtain the profile reported in Figures S1c and S1.d.

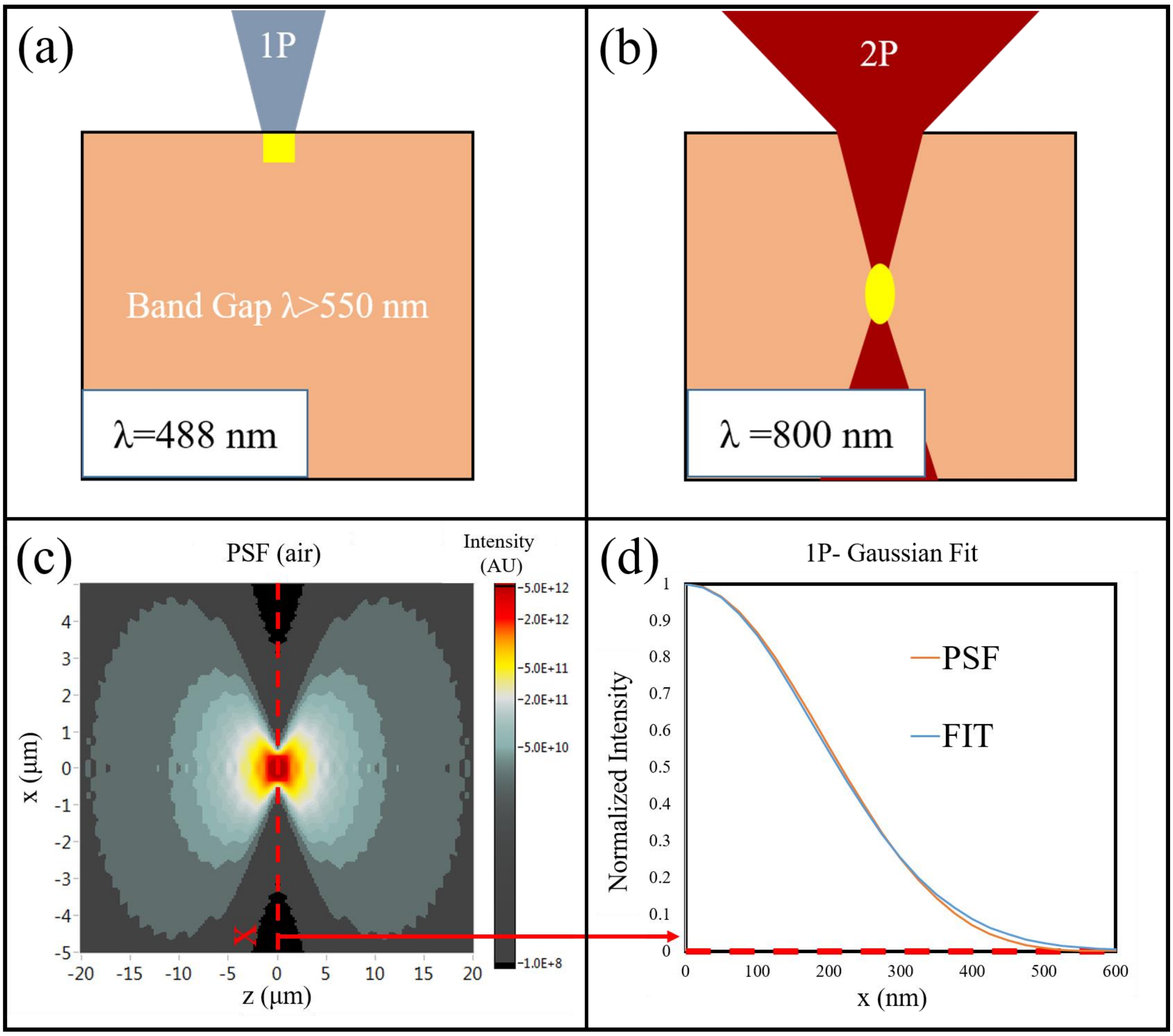

Figure S1 : Schematics of (a) normal (one-photon, 1P-488 nm–supra-bandgap) and (b) two-photon, 2P (800 nm-sub-bandgap) excitation (for $APbBr_3$ materials) microscopy and photobleaching. While the supra-bandgap light (1P) is absorbed by the halide perovskite within a few 100 nm, exponentially decreasing from the surface, (left), sub-bandgap light (2P) penetrates the crystal and is absorbed within the crystal. This behavior depends on the non-linear dependence of 2P absorption on light intensity. Due to the material's high refractive index, the focus of the light inside the crystal is shifted to deeper inside the material. This changes the energy deposition by 2P absorption. Accurate calculations are needed to calculate this aberration effect, and are reported in the following section. **(c)** I-P intensity distribution around the focus (point spread function - PSF) of an objective with NA=0.75 and effective NA=0.505. The 488 nm laser profile is indeed smaller than the objective back aperture diameter. (d) Gaussian fit of the PSF on the x axis. The PSF is normalized to its maximum value. The fitted σ of the Gaussian is 181.3 nm.

SI.3. FRAP procedure

A FRAP experiment is usually composed of 3 steps: 1- obtain the PL image before damage (Figure S2-A), which gives the reference PL signal. 2- cause damage (bleaching) with high laser power (Figure S2-B); 3- monitor PL recovery over time (at imaging intensity, which is << than bleaching intensity) (Figure S2-C-D). The intensity of the bleaching can be varied. The maximum laser power that is used defines the maximum bleaching power. Commonly the laser power can be tuned with an accuracy of 0.1% of the maximum laser power.

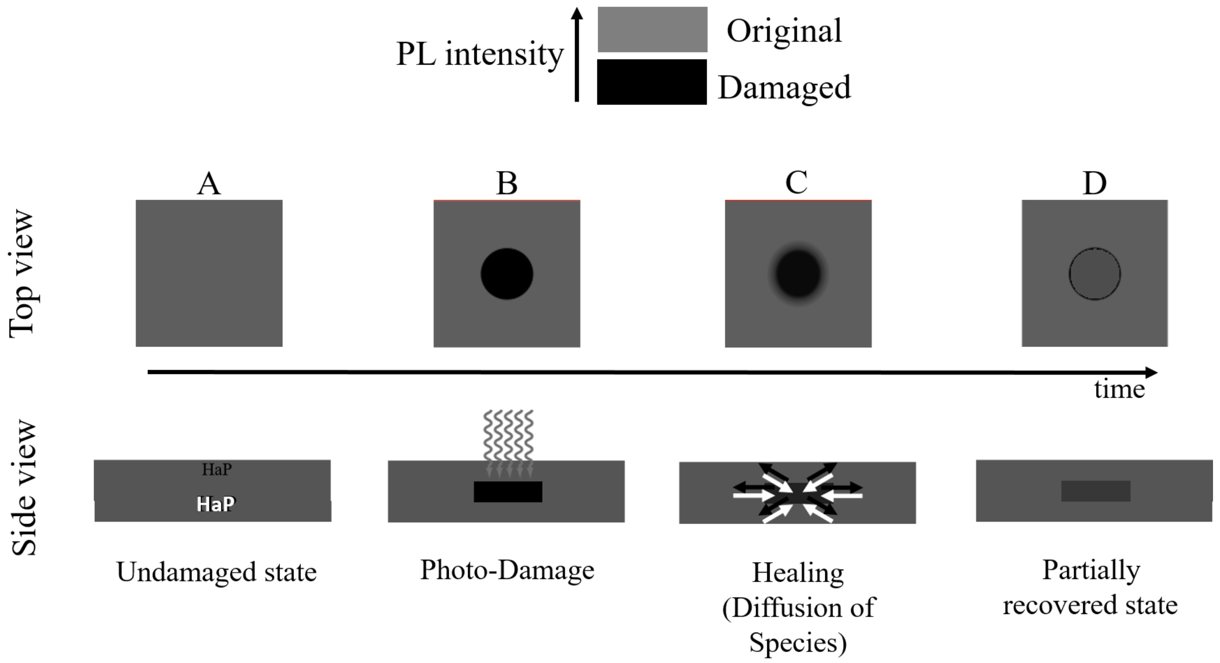

Figure S2 : The successive steps of the FRAP experiment; cf. SI.3 text for explanation.

SI.4. Definition of the value of $\boldsymbol{\varepsilon}_{\mathbf{sun}}$.

$\boldsymbol{\varepsilon}_{\text{sun}}$ is defined as the energy per unit of volume (J/m^3) that is absorbed at and near the surface by MAPbBr$_3$ upon exposure to AM1.5G solar radiation in one second. In the following we use MAPbBr$_3$ as example and note that results for FAPbBr$_3$ and CsPbBr$_3$ will differ slightly values their absorption is not exactly the same as that of MAPbBr$_3$.

$$\text{(a)}\ \varepsilon_{sun} = \left(\frac{dI_{sun}}{dz}\right)_{surf} \cdot \Delta t_0$$

$$\text{(b)}\ \left(\frac{dI_{sun}}{dz}\right)_{surf} = \int_{200\,nm}^{1600\,nm} \alpha_{\text{MAPbBr3}}(\lambda) * I_{Sun}(\lambda)\, d\lambda$$

with $\alpha_{\text{MAPbBr3}}(\lambda)$ the wavelength-dependent 1P absorption coefficient of MAPbBr$_3$^{2} and $I_{Sun}(\lambda)$ the wavelength-dependent solar intensity (from[26]), where 200 and 1600 nm are taken to (over)assure that all solar radiation is included. $\left(\frac{dI_{sun}}{dz}\right)_{surf}$ is the solar power/unit volume, absorbed at the surface in the very first layer of material; with $\Delta t_0 = 1$ sec, $\boldsymbol{\varepsilon}_{\text{sun}} = 2.2\cdot 10^9$ J • m^{-3}. This value defines the density of solar energy deposited in a MAPbBr$_3$ crystal or thin film in the top layers in one second and can be considered as a volume-normalized dose.

Note that AM 1.5 radiation, integrated between 200 (again to (over)assure that all radiation is included, as most UV radiation < 300 nm is absorbed by ozone) and 530 nm (corresponding approximately to the onset of MAPbBr$_3$ absorption) is $\int_{200\,nm}^{530\,nm} I(\lambda)\, d\lambda = 300\ W\ \bullet\ m^{-2}$. Because of the high 1P absorption coefficient of MAPbBr$_3$ at 500 nm, $\sim 10^7\ m^{-1}$, the density of energy actually absorbed by the material quickly decays while penetrating into it. One can make an approximate evaluation considering that all the 300 W • m^{-2} of photon energy gets absorbed in the first 200 nm of the crystal (an overestimate as ~ 90% of the absorbable light is absorbed in that thick a film). By this simple calculation we obtain $\boldsymbol{\varepsilon}_{\mathrm{sun}} = 1.5\cdot10^{9}$ J • m^{-3}. However, for our discussion we keep the formally correct value of $\boldsymbol{\varepsilon}_{\mathrm{sun}} = 2.2\cdot10^{9}$ J • m^{-3}.

SI.5. Laser intensity and deployed energy in 2-P and 1-P experiments.

In the Supplementary Information of ref.[1] we discuss the amount of aberration of 800 nm light inside a MAPbBr$_3$ single crystal. The evaluation of the aberration and, consequently, of the real absorption of light and energy by the bleaching treatment, depends on various instrumental parameters. Calculations that take into account all the critical parameters for 2P absorption were performed and the results reported in ref. [1].

Following the same notation as that used in the SI of [1] we define the value for Sup_{488nm}. As before[1] the pixel size is smaller than the light resolution. Because of this when the laser is directed to the following pixel, the preceding one is still in the focus of the objective and is exposed to laser light. The Sup_{488nm} factor is a multiplicative factor that corresponds to the ratio between the actual absorbed energy in the area of the pixel and the energy that would be absorbed in the area of the pixel if the laser would have been on when pointing at the pixel only and then switched off when pointed at the following pixel. In our experiments the pixel size is 250 nm, $\Delta t =$ 8.0 µsec and σ the standard deviation of the Gaussian profile (equal to 181.3 nm) as imposed by the instrument. Considering these parameters we obtain a value of $Sup_{488nm} = 3.30$. Using the values obtained by the PSF (point spread function cf. SI.2) simulations and considering all the mentioned conditions and the maximum incoming time-averaged laser power equal to 880 µW for the 1P microscope and 120 mW for the 2P microscope we have:

For the 1P case

$$\text{(a) } W_{sun}^{1P} = \frac{\frac{Max(PSF)_{1P}}{2} * LP_{488} * \Delta t_{1P} * \alpha_{MAPbBr3}^{488} * Sup_{488nm}}{\boldsymbol{\varepsilon}_{\mathrm{sun}}} = 670\ (\boldsymbol{\varepsilon}_{\mathrm{sun}})$$

where W_{sun}^{1P} is the energy density deposited by one bleaching cycle at 100% of the laser power (LP_{488}); $Max(PSF)_{1P}$ is the maximum value of the Pointing vector as calculated by the simulation in SI.2 (the division by 2 comes from the averaging over the time of its oscillating value); Δt_{1P} is the pixel dwell time; $\alpha_{MAPbBr3}^{488}$ is the 1P absorption coefficient of MAPbBr$_3$ at 488 nm; Sup_{488nm} was defined above and $\boldsymbol{\varepsilon}_{\mathrm{sun}}$ is the above-mentioned value of the density of energy absorbed at the surface in one second by $MAPbBr_3$. At lower percentage of the laser power (X%) a value equal to $\frac{X}{100} * W_{sun}^{1P}$ is deposited on the sample.

For the 2P case, instead, we have

$$\text{(b) } W_{sun}^{2P} = \frac{\frac{3}{8} Max(PSF)^2{}_{2P} * LP_{800}^2 * \frac{\tau_{rep}}{\tau_{pulse}} * \Delta t_{2P} * \beta_{MAPbBr3}^{800} * Sup_{800nm}}{\boldsymbol{\varepsilon}_{\mathrm{sun}}} = 770\ (\boldsymbol{\varepsilon}_{\mathrm{sun}})$$

with W_{sun}^{2P}, the energy density deposited by one bleaching cycle at 100% of the laser power (LP_{800}); $Max(PSF)_{2P}$ the maximum value of the Pointing vector as calculated by the simulation in[1] (the multiplication by 3/8 comes from the averaging over time of the square of its oscillating value) ; Δt_{2P} is the pixel dwell time; $\beta_{MAPbBr3}^{800}$ is the 2P absorption coefficient of $MAPbBr_3$ at 800 nm; Sup_{800nm} is as Sup_{488nm}, the multiplication factor that was defined above; τ_{rep} is the inverse of the pulse repetition rate of the laser (12.5 ns); τ_{pulse} the duration of the pulse (140 fs) and $\boldsymbol{\varepsilon}_{\mathrm{sun}}$ the above-mentioned value of the density of energy, absorbed at the surface in one second by $MAPbBr_3$. At a lower fraction of the laser power (X%) a value equal to $\left(\frac{X}{100}\right)^2 * W_{sun}^{2P}$ is deposited in the sample to take the quadratic dependence of the 2P absorption on the laser power into account.

In the 1P case, actually, the absorbed energy is captured by the (hot) carriers which loose part of their energy (0.2 eV) by scattering heating the system. The carriers then recombine ether through traps or through bimolecular recombination producing more heat (2.34 eV). Therefore, the volume in which the heat is released has the potential to be larger than the volume of absorption of the light accordingly to the carriers' diffusion length. Halide perovskite single crystals have shown to have diffusion length of the order of multiple μms with values reaching[3] the 175 μm and 3 mm. Taking the most unfavorable case found in literature[4] (which gives rise to the highest temperature), we consider the diffusion length of the carriers to be 3 μm. We can then consider the energy absorbed from the material to be released with a distribution roughly Gaussian with inflection point at 3 μm from the maximum absorption in the x,y,z direction. In the 1P case we can consider the 3 μm form the surface and from the center of the laser spot.

Concretely, if light is focused on a 272 nm × 272 nm (diffraction limit) spot and completely absorbed in around 200 nm depth, heat is released to x,y distance and depth that are actually 15 times larger. This means that the previously calculated W_{sun}^{1P} should actually be divided for a factor 15^3. It is our opinion that the actual diffusion length in our crystal is actually smaller than

3 μm. Measuring its exact value in the relevant conditions (partially illuminated, with non-uniform carrier concentration, sample) is not trivial and is out of the scope of this article.
In the 2P case a similar effect of diffusion of the energy should be considered. However, the 2P absorption is more diffuse in the volume. This means that the dilution of the energy density calculated in the 2P case is less pronounced than the one calculated in the 1P case.
This effect provides a likely explanation for the discrepancy between the $\boldsymbol{\varepsilon}_{\text{sun}}$ values at which we see the first damage in the 2P and 1P cases bringing the actual value of energy density in the 1P case down to the 2P case (if not lower).

SI.6. Evaluation of the temperature during the FRAP experiment.

The temperature rise upon bleaching can be calculated knowing the thermal parameters of the halide perovskites. The light deploys energy with a distribution that is dependent on light focusing and light concentration. In the previous section, we calculated the energy released by the laser during a bleaching cycle. We also mentioned that considering the distribution of energy release equivalent to the light absorption distribution is an inexact approximation. In fact, the charges recombine with a Gaussian profile with inflection point of at least 3 μm.

From the diffusion equation

$$\text{(c) } \Delta^2 T + \frac{HS}{\rho\, C_p} = \frac{1}{\alpha}\frac{\partial T}{\partial t}$$

With T as temperature and α the thermal diffusivity (with k the thermal conductivity, ρ the density and C_p the heat capacity of the material)

$$\text{(d) } \alpha = \frac{k}{\rho\, C_p}$$

Considering the values for $MAPbBr_3$ of heat capacity[5] (180 $J{\bullet}K^{-1}{\bullet}mol^{-1}$ which divided for the molecular weight (MW=479 g•mol) becomes 0.375 $J{\bullet}K^{-1}{\bullet}g^{-1}$), the mass density[6] (ρ=3.83 $g{\bullet}cm^{-3}$), heat conductivity (measured[7] to be 0.44 $W{\bullet}m^{-1}{\bullet}K^{-1}$ comparable with the one of water) we have a product $\rho\, C_p = 1.44 * 10^6 \text{ J} \bullet \text{K}^{-1} \bullet \text{m}^{-3}$. So $\alpha = 3.05\ * 10^{-5}\, m^2 \bullet s^{-1}$.

If we consider all the heat injected into the system instantaneously at time t’ from a single point of coordinates x’, y’ and z’ we have as a solution of the heat equation:

$$\text{(e) } \Delta T(x, y, z, t) = \frac{Q_{instant}}{\rho\, C_p} * \frac{1}{(4\pi\alpha(t-t'))^{\frac{3}{2}}} Exp\left(-\frac{((x-x')^2+(y-y')^2+(z-z')^2)}{4\alpha(t-t')}\right)$$

If the heat is not released instantaneously but over time then it is possible to rewrite the equation as (with the time t’=0 the for the first released heat):

$$\text{(f)}\ \ \Delta T(x,y,z,t) = \int_0^t dt' \frac{Q(t')}{\rho\, C_p} * \frac{1}{(4\pi\alpha(t-t'))^{\frac{3}{2}}} Exp\left(-\frac{((x-x')^2+(y-y')^2+(z-z')^2)}{4\alpha(t-t')}\right)$$

The heat can also be released not in one point only but can have a distribution:

$$\text{(g)}\ dT(x,y,z,t) = \int dz' \int dy' \int dx' \int_0^t dt' \frac{Q(x,',y',z',t')}{\rho\, C_p} *$$

$$\frac{1}{(4\pi\alpha(t-t'))^{\frac{3}{2}}} Exp\left(-\frac{((x-x')^2+(y-y')^2+(z-z')^2)}{4\alpha(t-t')}\right)$$

We can describe the heat source distribution as Gaussian with σ the flex point distance and P the total energy deployed per unit of time.

$$\text{(h)}\ Q(x',y',z') = \frac{P}{(2\pi\sigma^2)^{\frac{3}{2}}} Exp\left(-\frac{\left(x'^2+y'^2+z'^2\right)}{2\sigma^2}\right)$$

This distribution of heat can be considered as the heat originated from a point that already had some time τ to diffuse (this is because Gaussians evolve into Gaussians and a point injection of heat can be seen as heat injected with Gaussian distribution into an extremely small, point like, volume).

$$\text{(i)}\ \ \tau = \frac{\sigma^2}{2\alpha}$$

Considering $\sigma = 2.5\ \mu m$ we would have a time $\tau = 10^{-7} s$. The heat distribution at the end of the bleach $t > t_{bleaching}$ will then be equivalent to the heat distribution of the same system where the energy, instead of being injected with a Gaussian distribution at time t’ was injected in a point-like distribution at time t’-τ.

It is then possible to estimate the temperature at the end of the bleaching cycle and its evolution (to calculate the temperature during the cycle more calculations are needed) over time. The temperature at the end of the bleaching cycle (whose timespan is $t_{bleaching}$) is the maximum temperature that the system experiences, therefore there is no need to assess the temperature during the bleaching cycle.

Then, with $P(t')$ the total power absorbed by the system, it is possible to write:

$$\text{(j)}\ \ \Delta T(x,y,z,t) = \int_{-\tau}^{-\tau+t_{bleaching}} dt' \frac{P(t')}{\rho\, C_p} * \frac{1}{(4\pi\alpha)^{\frac{3}{2}}} *$$

$$\frac{1}{(t-t')^{\frac{3}{2}}} Exp\left(-\frac{((x-x')^2+(y-y')^2+(z-z')^2)}{4\alpha(t-t')}\right)$$

If we consider the point at the center of the Gaussian (x=y=z=0) ant that the absorbed power is constant with the time, the integral is of easy solution:

$$\text{(k) } \Delta T(x,y,z,t) = \int_{-\tau}^{-\tau+t_{bleaching}} \frac{dt'}{(t-t')^{\frac{3}{2}}} * \frac{P}{\rho\, C_p (4\pi\alpha)^{\frac{3}{2}}}$$

$$\Delta T(x,y,z,t) = \left[\frac{2}{\sqrt{t-t'}}\right]_{-\tau}^{-\tau+t_{bleaching}} * \frac{P}{\rho\, C_p (4\pi\alpha)^{\frac{3}{2}}}$$

$$\Delta T(x,y,z,t) = 2\left[\frac{1}{\sqrt{t-t_{bleaching}+\tau}} - \frac{1}{\sqrt{t+\tau}}\right] * \frac{P}{\rho\, C_p (4\pi\alpha)^{\frac{3}{2}}}$$

Considering $t = t_{bleaching}$ the instant with the maximum temperature is:

$$\text{(l) } \Delta T(x,y,z,t) = 2\left[\frac{1}{\sqrt{t+\tau}} - \frac{1}{\sqrt{t_{bleaching}+\tau}}\right] * \frac{P}{\rho\, C_p (4\pi\alpha)^{\frac{3}{2}}}$$

substituting the numerical values. For the 1P case we have $P(100\%) = 0.88 * 10^{-3} W$ and $t_{bleaching} = 8 * 10^{-6}\ s$.

$$\text{(m) } \Delta T(x,y,z,t) = 2\left[\frac{1}{\sqrt{1*10^{-7}\ s}} - \frac{1}{\sqrt{8.1*10^{-6}\ s}}\right] * \frac{0.88*10^{-3} W}{1.44*10^{6}\ \mathrm{J{\bullet}K^{-1}{\bullet}m^{-3}}} * \frac{1}{(3.8*10^{-4} m^{2}{\bullet}s^{-1})^{\frac{3}{2}}}$$

$$\Delta T(x,y,z,t) = 2\left[3162\ s^{\frac{-1}{2}} - 351 s^{\frac{-1}{2}}\right] * 0.88 * 10^{-3} W * 9.25 * 10^{-2} (\mathrm{K} \bullet \mathrm{s}^{\frac{3}{2}} \bullet \mathrm{J}^{-1})$$

$$\Delta T(x,y,z,t) = 2\left[2811\ s^{\frac{-1}{2}}\right] * 8.14 * 10^{-5} \left(\mathrm{K} \bullet \mathrm{s}^{\frac{1}{2}}\right) = 0.45\ K$$

Therefore, the amount of heat released is negligible.

Actually, in the 1P case the geometry is slightly different from the one considered here. Heat diffusion occurs in only half (lower part – crystal corresponding) of the space. To take this into account is sufficient to consider that all the heat that diffused trough the surface is mirrored back into the perovskite crystal. The heat in the perovskite will then be doubled in respect of the current calculation bringing the temperature rise to 0.9 K.

For the 2P case, the calculation is also an approximation since the volume in which the energy is absorbed is actually larger, cylindrical like, than the one considered here. However, we do not expect qualitative differences in the temperatures since the considered volumes and energies are anyway similar.

We note that measuring transient temperature variations inside a material is a real technological challenge. While in principle possible (one can think of equipping the confocal microscope with means to sense the thermal-IR emission, during bleaching, but, as heat diffusion is relatively rapid, meaning that the signal would vary rapidly with the time), this needs detection with extremely high sensitivity; we do not know of existing or easily adaptable experimental setups that will allow such an evaluation.

To conclude, it has to be noted that the recombination dynamics is in the order of 5-10 ns, which is of the same order of the repetition time in the 2P experiment. Even if the 2P laser has pulses of 140 fs the heat release is mainly in the time-scale of the carrier recombination which, as we already mentioned, is in the same range of the pulse repetition rate. We can then neglect the decaying dynamics and consider the energy of the laser to be deployed uniformly in time while the laser is focused on the pixel with an error of few degrees.

We add also some observation that can be a starting point for future work, that supports the validity of our calculation. Firstly, we did not find any difference of the 2P-PL at 25°C, after keeping the temperature of the single crystal at +100°C for 1 hour and then cooling back to +25°C. Thus, for damage due to temperature variations to affect the PL, the local temperature of the sample should be > 100°C. We also performed experiments, similar to the ones we report as 2P in Fig. 1, while the sample is at different temperatures and find that the higher the temperature (+50°C, +60°C, +80°C, +100°C) the lower the PL after bleaching. Thus, bleaching at 16% 2P-LP, in $MAPbBr_3$ leads to PL decrease as the temperature increases, instead of PL increase, as is the case at RT. If the bleaching increases the temperature significantly (more than 100°C) then an initial temperature difference before bleaching (passing from +25°C to +50°C) should not cause the photodamage to be qualitatively different. The temperature after bleaching should be, indeed, anyway elevated. The strong dependence of the bleaching effect on the initial temperature suggests that the photoinduced degradation happens at temperatures similar to the ones before bleaching.

Finally, we conclude with some observation relevant for section 3 of the main text. To create samples for AFM and SEM analysis, photobleaching was performed 100 times successively over the same area. These photobleaching cycles happened with a 10 sec delay between each other. This means that any direct or indirect physical temperature effect has 10 seconds to dissipate before the next bleaching cycle. This is likely, because we just showed that the expected temperature increase is < 1 K / bleaching cycle.

We now calculate the temperature change expected 10 seconds after the end of the bleaching cycle. Using equation (e) above and assuming all the energy initially released in a point at the origin of the axis at t=0 (a condition that is much more stringent than what was used for the more realistic case, calculated from eqn. (m) above) we can obtain a maximum temperature at the origin after 10 seconds of

$$\text{(n)}\ \mathit{\Delta} T(x,y,z,t) = \frac{Q_{tot}}{\rho\, C_p} * \frac{1}{(4\pi\alpha t)^{\frac{3}{2}}} Exp\left(-\frac{0}{4\alpha t}\right) = \frac{0.88*10^{-3} W*10^{-5} s}{1.44*10^{6}\ \mathrm{J{\bullet}K^{-1}{\bullet}m^{-3}}} * \frac{1}{(3.8*10^{-4} m^{2} {\bullet} s^{-1} *10\ s)^{\frac{3}{2}}} = 2.6*10^{-8} K$$

which is absolutely negligible. Each of the 100 bleaching cycles thus acts on a material that is, temperature-wise, the same before the first and the 100th bleaching cycle. As the lifetime of the minority carriers is also much shorter than 10 seconds, the same consideration is valid for the photogenerated carrier density.

However, in contrast to the physical effects of the laser pulse and absorption by the HaP, the chemical effects can be cumulative and damage can accumulate, if the probability for back reaction is small (high activation energy) or disappears (e.g., one of the reaction products escapes).. This effect it is similar to what can happen during normal operation of solar cells, i.e., prolonged illumination, accompanied by surface chemistry (cf. also Fig. 5 in the main text).

SI.7. Spectra and FLIM measurements.

The spectra and FLIM measurements were recorded with the same 2P confocal microscope used for the FRAP experiments. Spectra were recorded with the Zeiss 880 LSM detector with a 3 nm spectral resolution, using the same laser settings as those used in the FRAP experiments. With those settings the acquisition time of a single image is long (~5 min), because of the need to repeat the imaging for every wavelength. The crystals were exposed to different bleaching cycles than those used to determine the self-healing recovery and threshold of damage. In particular, the crystals were bleached 10 times to increase the time needed to heal the damage and avoid undesired artifacts. The spectra were taken successively. Repeating the data acquisition just after the first time did not give differences in the recorded spectra. For FLIM, a fast Big2 GaAsP detector was used. The pixel dwell time had to be increased to collect a sufficient number of photons to define a decay curve separated into 256 time-steps. A pixel dwell time of ~40 µs was used and the scans were repeated for a total of 16 times to reach the desired photon quantity for a total acquisition time of 120 sec/image.

Thus, the images reported in Figures 2b, 2c in the main text were collected after bleaching the single crystals with 10 bleaching cycles. Laser powers of 6% and 14% were used to bleach the Cs sample on the surface, 15% and 22% for bleaching it in the bulk. For MA, laser powers of 10% and 14% were used to bleach the surface and 18% and 26% for bleaching in the bulk. The difference between the values of the bleaching laser power in the bulk and on the surface is due to the above-described aberration effect when the microscope is focused in the bulk.

The recorded decay curves were analyzed with the SPCImage software from Becker & Hickl GmbH. Because the repetition rate of the pulsed laser (12.5 ns) is in the same time scale as the decay, the program takes into account the incomplete decay of the PL, when a new pulse impacts the crystal again. A bi-exponential decay is used to fit the data:

$$\text{(n)}\ PL(t) = A1 * e^{\frac{-t}{\tau 1}} + B2 * e^{\frac{-t}{\tau 2}}$$

with τ_1 and τ_2 the shortest and longest decay times, *A1* and *B2* the prefactors for the respective fast and slow decays. This fitting is adequate to describe a simple model where the PL decay is determined by the trapping and trap-assisted recombination of the excited minority carriers. Under the conditions considered, the electron-hole recombination that leads to the PL is not the dominant recombination mechanism at any moment of time of the decay. Defining k_{bi} as the kinetic constant of the bimolecular recombination, n_M the majority carrier concentration, k_{trap} the kinetic constant of the trapping of the minority carrier and k_{recomb} the kinetic constant of the recombination between the majority carriers and the trapped minority carriers (see figure S6-left) this condition corresponds to

$$\text{(o)}\ \begin{cases} k_{bi} n_M \ll k_{recomb} \\ k_{bi} n_M \ll k_{trap} \end{cases}$$

Whether these inequalities hold or not is verified in two ways 1) the obtained fitting parameters should not vary with increasing/decreasing laser power, used to excite the PL for the FLIM experiment (which, if a bimolecular recombination mechanism were present, should modify τ_1 , because of the increasing density of both carriers with increasing absorbed radiation). 2) in the bleached volumes/areas, the obtained fitting parameters vary with respect to the backgrounds in ways that cannot be modeled by a bimolecular recombination decay. In Figure S3 we report, similarly to what is shown in Figures 2b and 2c of the main text, the PL and the lifetime (τ_2) – corresponding to trap-assisted recombination – of the bleached areas for the Cs and MA samples both on the surface and in the bulk. This time however, we also report the shorter lifetime (τ_1) – corresponding to trapping – as well as the value of the A1 parameter (cf. eqn. (i)) of the faster decay (A1 and B2 are normalized to 100% → B2=100%-A1). In the figure, each of these parameters is mapped with a color map. For each experiment the colors have different meaning and intervals which is reported in the left column. As is seen readily, A1 and τ_2 vary substantially

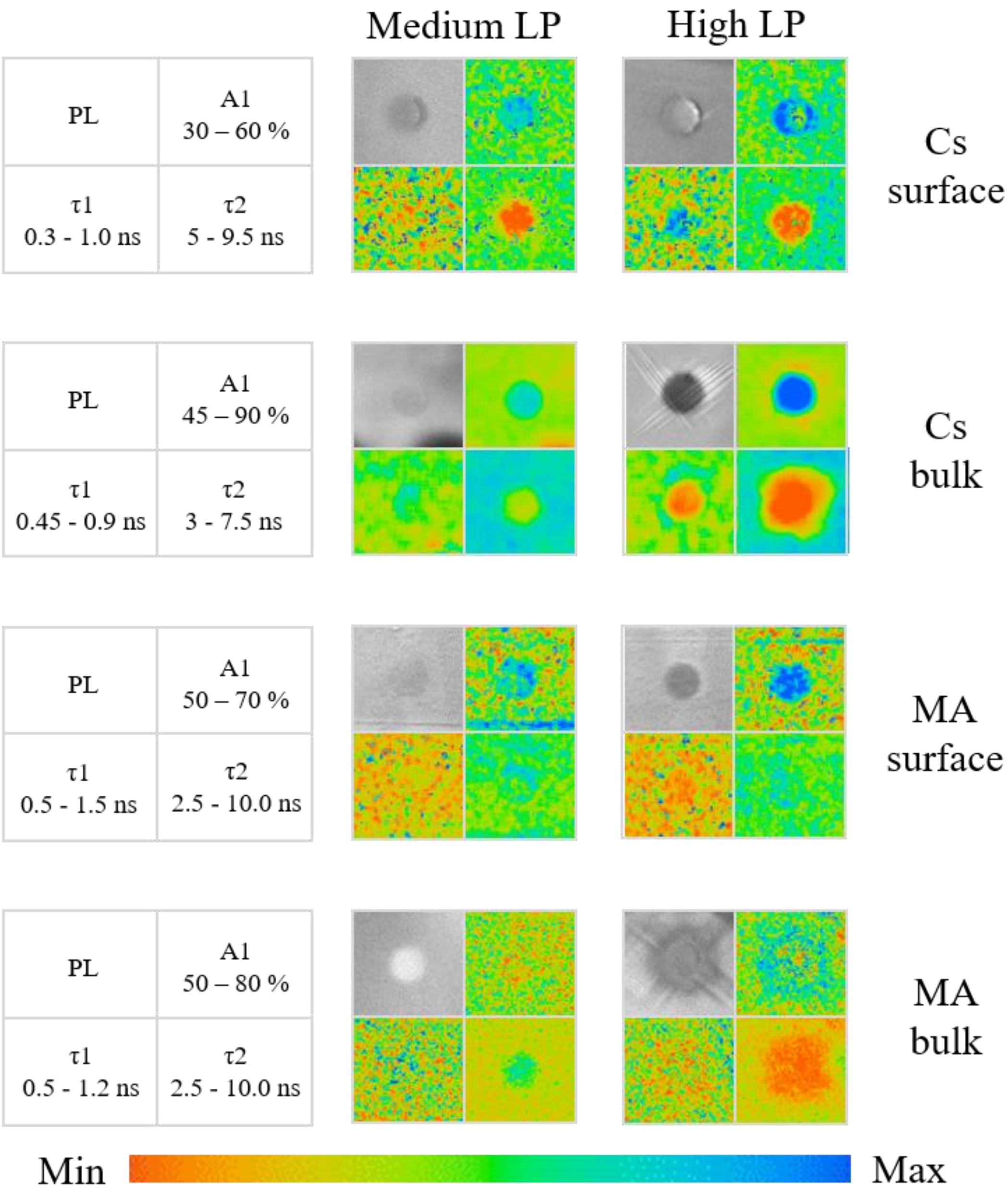

Figure S3 : Values of the parameters of the bi-exponential fits (equation *(g)*) of the PL decay for $CsPbBr_3$ and $MAPbBr_3$ crystals at their surfaces and in their bulk. Each square in the 4 squared images in the MIDDLE and RIGHT columns, is made up of the values of PL (upper left corner), A1 (upper right corner), τ1 (lower left corner) and τ2 (lower right corner) for the different settings and samples. The LEFT column then gives the minimum and maximum values for each corresponding square in the 4 squares **in the MIDDLE and RIGHT** columns. These correspond respectively to intermediate and high intensity bleaching. The bar at the bottom provides the color code for the images.

after bleaching (esp. for the Cs compound), while τ_1 is not strongly modified. In a one trap model (Figure S4a) we can assume two different probabilities of trapping k_{trap} and recombination through the trap k_{recomb} (probability for the electron in the trap to recombine with a hole in the valence band, assuming electrons as minority carriers). In such a case, we can obtain the reported changes in the values of the fitting parameters when increasing the number of traps N_t (or reducing them for the case which shows an increased luminescence). This is shown clearly in Figure S.4b where we simulate the values of A1, B2 τ_1 and τ_2 as function of the ratio between the trap

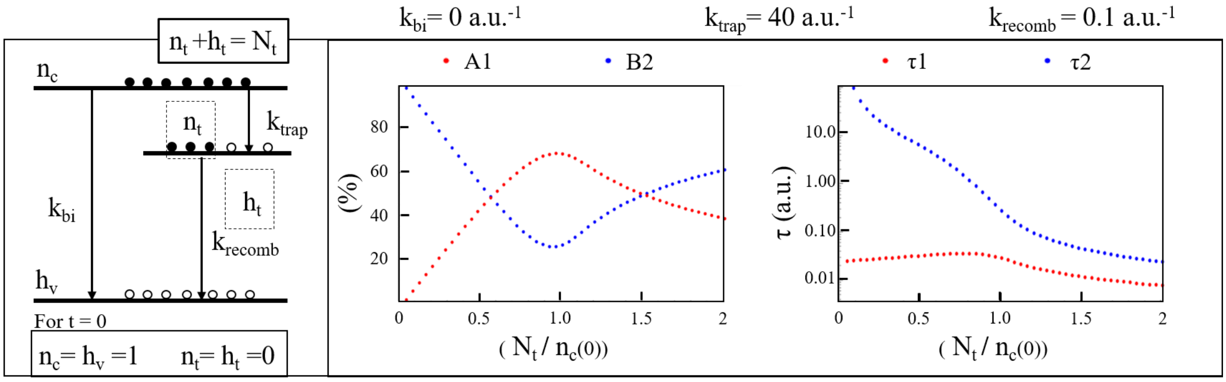

Figure S4 : (**left**) Scheme of the model used to derive equations in (i). (**center**) % of the first (A1) and second (B2) component of the fitting through a bi-exponential decay of the solution of equations (g). The two components are shown as function of the ratio between the number of traps (N_t) and the initial electron density, n_c. As can be seen, the component of the shortest lifetime (red) is the highest for a ratio approximately equal to 1. In our case, the results are consistent with an initial situation where the number of traps is smaller than the number of carriers. After the bleach, the number of traps increases (decreases for MA – medium power). Comparing with Figure.S3 is possible to see how the values of A1, B2, τ1 and τ2 follow the tendency described here for trap numbers for N_t/n_c<.1 increasing (decreasing for MA – medium power) after the bleach. (**right**) shortest (red) and longer (blue) decay time of the fitting through a bi-exponential decay of the solution of equations (i). The two times are shown as function of N_t/n_c. As can be seen the longest lifetime is the most sensitive to the variation of the number of traps while the shortest one does not vary much. This behavior is also consistent with the results reported in Figure.S3.

concentration N_t and the number of photo-excited electrons in the conduction band n_c or holes in the valence band h_v at t=0 of the FLIM excitation. These fitting numbers were obtained by fitting of the calculated PL obtained by the described model. In particular, the PL is proportional to $n_c * h_v$, the product of electron and hole densities. To obtain the value of this product we solved the following system of equations, valid for an intrinsic semiconductor with a single trap level:

$$\text{(p)} \begin{cases} \dfrac{dn_c}{dt} = -k_{trap} * n_c * h_t - k_{bi} n_c * h_v \\ \dfrac{dn_t}{dt} = k_{trap} * n_c * h_t - k_{recomb} * n_t * h_v \\ \dfrac{dh_v}{dt} = -k_{recomb} * n_t * h_v - k_{bi} n_c * h_v \\ N_t = n_t + h_t \\ n_c(t=0) = 1 \\ h_v(t=0) = 1 \end{cases}$$

with n_t electrons and h_t holes in the trap level and $k_{bi} = 0$. By normalizing to the value of $n_c * h_v$ at t = 0 and fitting the graph with equation (g) we obtained the values A1, B2, τ_1 and τ_2.

As previously described, a bi-exponential decay is obtained in a situation in which the trapping process is much faster than the trap-assisted recombination. This corresponds to the condition $k_{trap} \gg k_{recomb} \gg k_{bi}$ in the equations (i). If $k_{trap} < k_{recomb}$, a substantially mono-exponential, k_{trap} determined, decay would be found. The parameters to obtain the evaluation of the fitted parameter are reported in Figure S4. Upon increasing the number of traps (when it is still lower than the number of excited carriers $\frac{n_t}{n_c(t=0)} < 1$) we see an increase of A1, a decrease of τ_2 and little variation in τ_1. This trend follows what we reported in Figure S3 for the Cs and Ma sample at high bleach intensity. In the case of MA of low bleaching intensity, the values behave in an opposite way, which, in this model, is interpreted as a decrease of the trap number.

SI.8. Detection of solvent molecules in single crystals.

Some of single crystals samples were analyzed through thermogravimetric analysis coupled mass spectroscopy (TGA-MS refer to the next paragraph for the experimental details). Crystals containing MA are usually synthesized in DMF, FA in a mix of DMF and GBL while Cs ones require DMSO. Crystal containing a mix of cation are synthetized in mixed solvents. In Figure S5 are reported the chromatograms of the molecules expelled by a $FAPbBr_3$ (Figure S5a, grown in a solution containing GBL and DMF) and a $Cs_{0.65}FA_{0.35}PbBr_3$ (composition evaluated though TGA - Figure S5b, grown in a solution containing GBL, DMF and DMSO) sample recorded between 320 ºC and 360 ºC respectively. The first (Figure S5a) reveals, besides the products of decomposition Triazine and HBr, clear traces of GBL and DMF. Adding DMSO in the crystallization solution causes DMSO to be also "dissolved" in the single crystal (Figure S5b). The measured MS spectra of DMF (Figure S5c), DMSO (Figure S5d), GBL (Figure S5e) and triazine (Figure S5f) that allowed identified the different solvent molecules are reported for completeness.

The decomposition product of $FAPbBr_3$ were identified as triazine and HBr. For $MAPbBr_3$ we could identify HBr and CH_3Br implying the formation of CH_3NH_2, NH_3 and $PbBr_2$ left on the surface. For none of the $APbBr_3$ we could identify the formation of Br_2. This does not exclude its formation under light-treatment since $PbBr_2$ is known to photodegrade.

Thermogravimetric Analysis Gas chromatograph mass spectrometer (TGA-GC/MS) experiments were performed with PerkinElmer 'Pyris 1' TGA, 'Clarus 680' GC and 'Clarus SQ 8 C' MS instruments. 5-10 mg of $FAPbBr_3$ and $Cs_{0.65}FA_{0.35}PbBr_3$ samples were subjected to a TGA oven, with a heating rate of 20 °C /min from 30 to 900 °C, under a nitrogen atmosphere (balance purge 80 mL/min; sample purge 20 mL/min) on alumina crucibles. The TGA was connected to a transfer-line (TL9000) of 'Red Shift' heated to 280 °C, connected to 100 µL loop. The gas

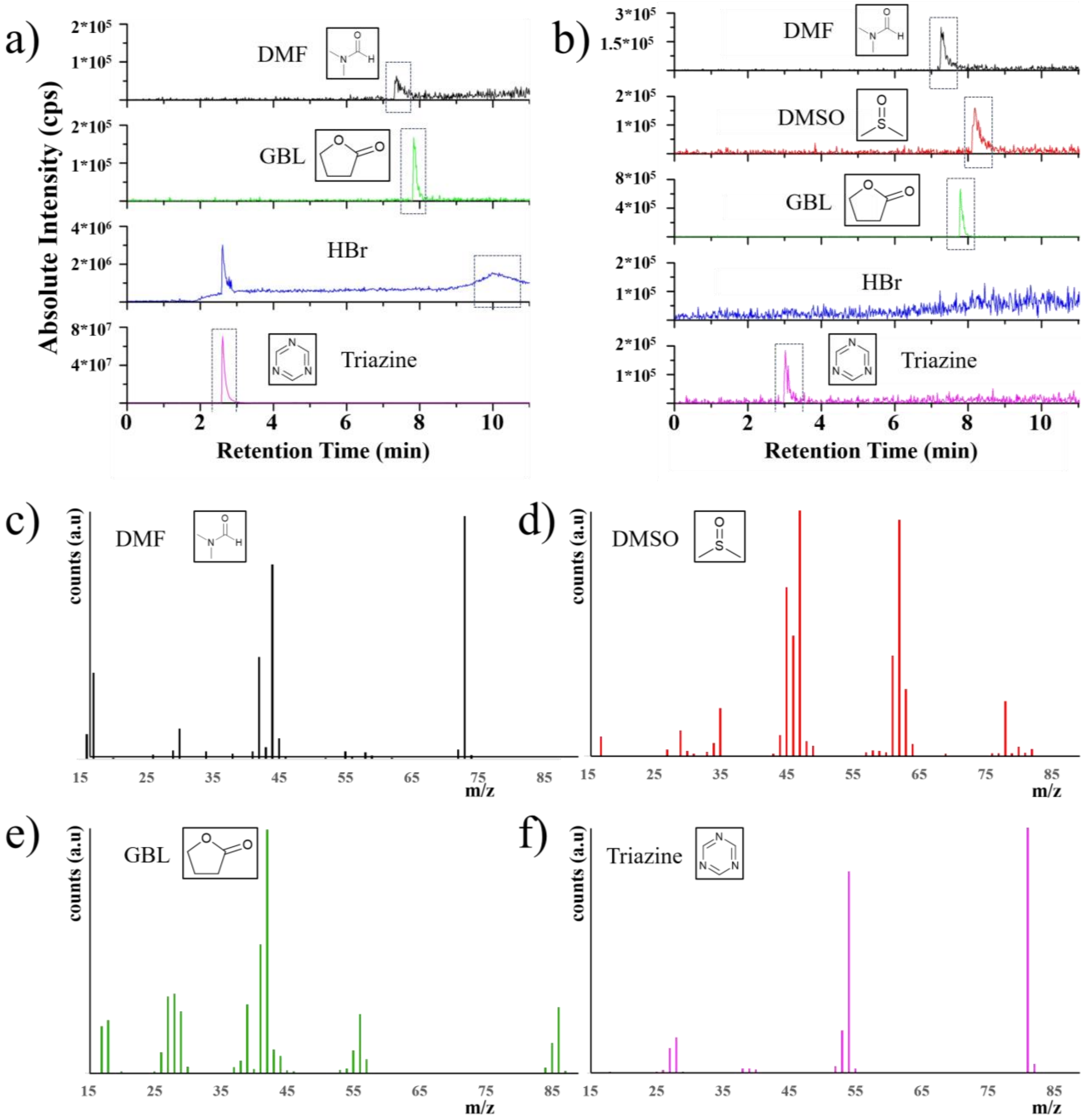

Figure S5: Chromatogram of the molecules expelled by a a) FAPbBr$_3$ and a b) Cs$_{0.65}$FA$_{0.35}$PbBr$_3$ single crystal between 320 ºC and 360 ºC. The different channels correspond to the different molecules identified by mass spectroscopy. The MS spectrum of c) DMF, d) DMSO, e) GBL and f) triazine are reported in black, red, green and purple respectively following the color-code of the chromatogram.

mixture was then separated over 5 MS (30 m x 0.25 mm) column using helium as a carrier gas at a flow rate of 1.0 ml/min. The column temperature held 5 min at 40 °C, then raised to 300 °C at 20 °C/min and held at 300 °C for 3 min. The mass spectrometer conditions were as follows: Electronic Impact ionization at 70 eV, source temperature 220 °C and GC transfer line 250 °C. Mass range 15−300 Da with 0.2 s dwell time. The data were collected and analyzed by GCMS PerkinElemer TurboMass software

SI.9. Computational Details and calculated structures.

All DFT calculations were performed using the Perdew-Burke-Ernzerhof (PBE)[8] form of the generalized-gradient approximation, augmented by dispersion terms calculated within the Tkatchenko-Scheffler (TS) scheme[9]. All calculations were performed using the Vienna ab initio simulation package (VASP)[10], a plane-wave basis code in which ionic cores are described by the projected augmented wave (PAW)[11] method. A plane-wave cutoff of 500 eV, 600 eV and 800 eV was used for the $CsPbBr_3$, $MAPbBr_3$ and $FAPbBr_3$ systems, respectively. A 10^{-6} eV/supercell convergence criterion for the total energy was used in all calculations.

3×3×3 supercells of the cubic $MAPbBr_3$ and $FAPbBr_3$ systems (a=5.92Å and a=5.97Å, respectively)[12] and 2×2×2 supercells of the orthorhombic $CsPbBr_3$ system (a=8.24Å, b=11.74Å, c=8.20Å)[13] were used in all calculations to mitigate defect-defect interactions. Consequently, a 2×2×2 k-point grid was used for all supercell calculations.

To introduce a MABr vacancy into the system a MA molecule and a nearby Br atom were taken out of the supercell. Similarly, in order to create an HBr vacancy, both MA and Br were taken out, and CH_3NH_2 was placed in the MA position. To create a CH_3NH_2 vacancy, MA was taken out of the supercell and an H atom was put in its place. To create a Br interstitial in all systems, a Br atom was added to the supercell in several different locations in order to determine its ideal, minimum energy position. All structures were then allowed to relax until the forces acting on the ions were below 0.015 eV/Å.

In the main text, we reported the structure for the positive charge interstitial defect of the $CsPbBr_3$, $MAPbBr_3$ and $FAPbBr_3$ systems. Defects can however be charged differently in function of the Fermi energy of the system. In Figure S5 we report the structure and electron density for the positive, neutral and negative Br interstitial defects in $MAPbBr_3$ ((a), (b) and (c) respectively) and $CsPbBr_3$ ((d), (e) and (f) respectively). We were not able to determine the equilibrium structures of the neutral and negative Br interstitial defects in $FAPbBr_3$ due to convergence issues. As can be seen the structure of the neutral and negative interstitial defects ((b) and (c), (e) and (f)) do not differ much. This suggests that the transition between the neutral and the negative state of the defect should be less energetically costly than the transition between the positively charged and the neutral one. The partial charge density associated with the defect is also not strongly

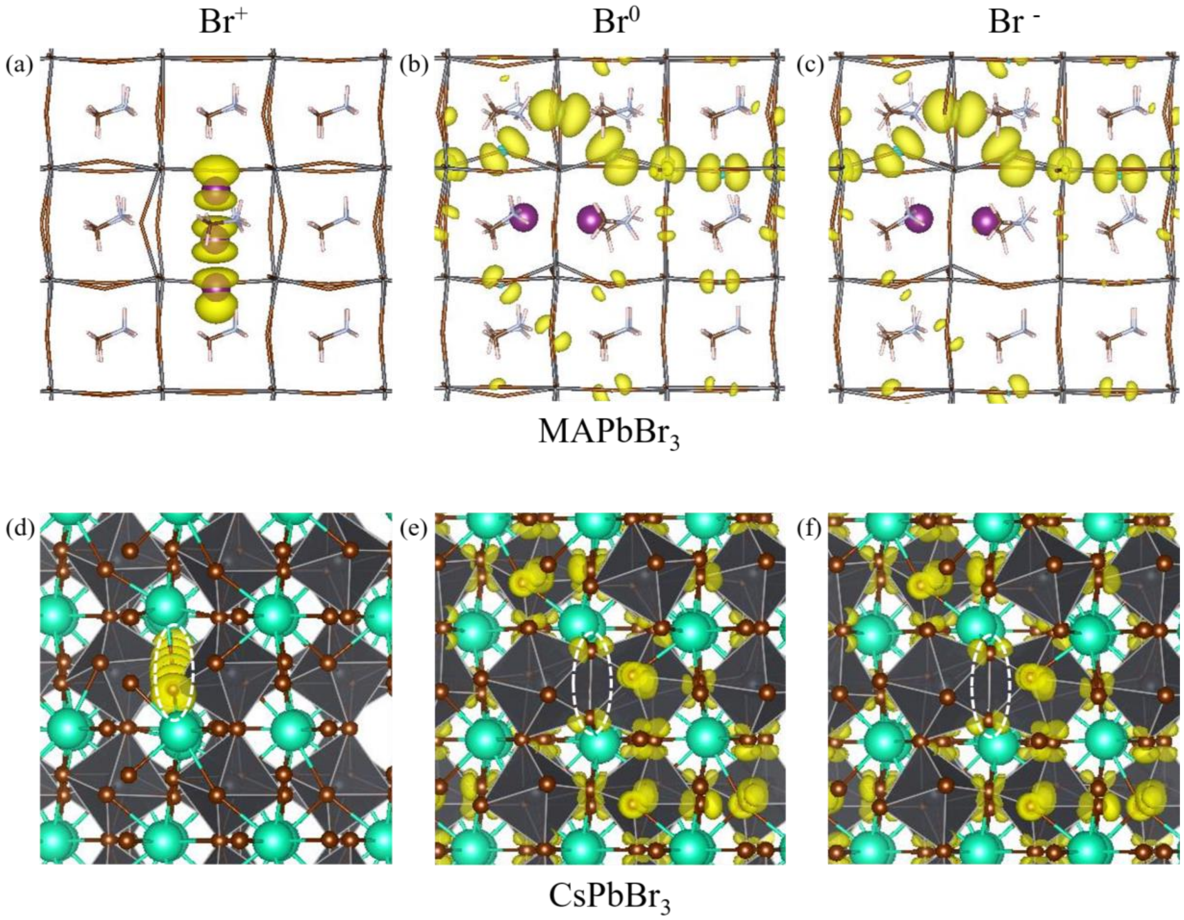

Figure S6: TOP: The minimum energy structure of $MAPbBr_3$ containing (a) Br_i^+ (b) Br_i^0 and (c) Br_i^-. The Br_i defects are marked in purple, and the yellow contours represent the partial charge density associated with the defect's eigenvalue.
BOTTOM: The minimum energy structure of $CsPbBr_3$ containing (d) Br_i^+ (e) Br_i^0 and (f) Br_i^-. The Br_i defects are marked by a dashed oval, and the yellow contours represent the partial charge density associated with the defect's eigenvalue.

affected by the added electron. In particular, no difference is easily identifiable for the Cs sample and any such difference is negligible for the MA sample.

SI.10. Halo around the bleached area for the 2P–high laser power experiment

When the laser power switches from 0% to the desired % during the scanning of the bleaching cycle there is a short transient in which the laser power is not at the desired value. This is due to the Acousto-Optic-Modulator governing the laser power, which leads to an error over 1-2 pixels. While acceptable for most 2P confocal microscopy applications, in our case, the laser power during this transient is in the range that produces the state of higher luminescence, causing the "ring-effect" in Figure.2b MA-Surf. High LP. Similar ring-effects were also found in other experiments with MA samples (not shown in this report).

SI.11. AFM measurement

AFM measurements were carried out in a Smart AFM (Horiba); Scans of 1000×300 pixels per image were made in the AC mode at a 0.5 Hz scanning speed, using a highly-doped silicon probe

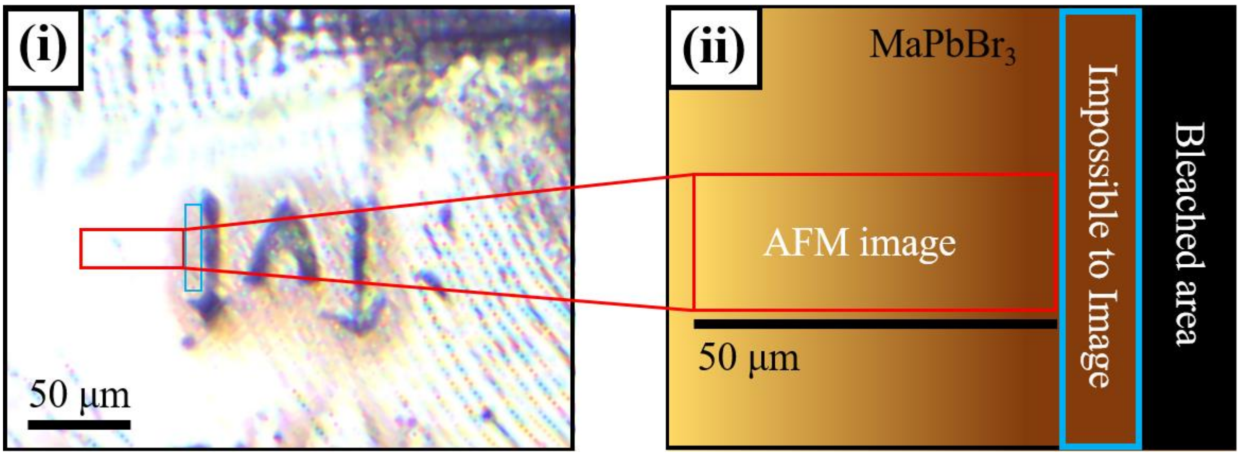

Figure.S7: (i) Optical image of the AFM scanned area. The direction of the arrows indicates the confocal scan direction. The letter A was used to indicate that in this bleaching spot the maximum laser intensity was used to perform the bleaching. Other experiments were performed with lower laser intensities but the results were less clear. (ii) Scheme of the position of the scanned area with respect to the bleached area.

(Olympus Co. AC160) with nominal resonance frequency and spring constant of 300 kHz and 26 N•m^{-1}. The sample was prepared by bleaching a long rectangular shape on the surface of a $MAPbBr_3$ single crystal. The bleaching was repeated 100 times in the 1P confocal microscope on the same area using 100% of the laser power. In this way, the halo around the bleached area reached farther away from that area and became identifiable/analyzable, which was not the case after one cycle. Attempts to use the AFM on the bleached area directly or close to the bleached area failed, probably because of the presence of the liquid-like phase, shown in Figure 4a of the main text. By measuring close to the bleached area, it was possible to obtain repeatable results. The distance between the bleached area and the right part of Figure 4a was estimated at 20 - 50 µm. An optical image of the bleached area (using the optical microscope, connected to the AFM) and a scheme of the positioning of the AFM image with respect to the bleached area are shown in Figure S7.

SI.12. Products of decomposition and formation of a liquid phase.

In the main text we described how the methylamine, produced by the 1-photon decomposition of $MAPbBr_3$, is probably the cause of the formation of $MAPbBr_3$ nanoparticles embedded in a liquid-like phase on the surface of the single crystal. Methylamine, CH_3NH_2, has been reported as one of the main decomposition products of $MaPbBr_3$, the others being CH_3Br, NH_3 and HBr and Br_2. Exposing the perovskite to CH_3Br and HBr does not produce any visible effect (tested in the laboratory), while exposure to CH_3NH_2 and NH_3 causes the formation of a liquid phase as reported in the literature[14]. We already discussed in the main text how the lower boiling point of NH_3 implies that most of the material that re-condenses and forms the liquid phase has to be CH_3NH_2. NH_3 would indeed evaporate much quicker. Exposure to Br_2 leads, instead, to whitening of the single crystals (as we could show in separate experiments in our laboratory).

In the case of $FAPbBr_3$, the decomposition leads to HBr, Br_2, NH_3 and 1,3,5-triazine $(HCN)_3$ [15,16], which is an heterocyclic aromatic ring compound with melting point around 80°C[17]. As the first three molecules have already been analyzed, the triazine can also be excluded to form any liquid phase because of its high melting point and its acidity (liquids form with basic methylamine). We note that, even if formamidine can be synthesized by the reaction of formamidinium with a strong base[18], it has not been reported hitherto as decomposition product of halide perovskites. In the case of $CsPbBr_3$, the only gaseous decomposition product is Br_2, which does not form any liquid with the perovskites.

SI.13. SEM and EDS measurements.

SEM and EDS studies were performed using a Zeiss Supra55 or Ultra55) field emission SEM equipped with Bruker XFlash 6, 60 mm detector. A landing voltage of 10 kV was applied on the samples, using a 30 μm aperture.

Quantification of the Pb:Br ratio requires calibration, because the e-beam affects different elements (and electronic transitions in an element) differently, leading to differences in X-ray emission. In particular, to obtain absolute atomic concentration ratios one has to have measured them from analytical chemistry tests on a reference material, which is similar to the sample. The EDS signal of each atom is multiplied by a calibration factor to give the chemically-measured atomic ratio in the reference sample. EDS can then be used to determine variations of the given ratio of elements in the sample of interest. In particular we have in expression (q) the relation between the real atomic ratio $\frac{Pb_{real}}{Br_{real}}$ and the EDS measured one $\frac{Pb_{EDS}}{Br_{EDS}}$.

$$\text{(q)}\ \frac{Pb_{real}}{Br_{real}} = \frac{cal_{Pb}}{cal_{Br}} * \frac{Pb_{EDS}}{Br_{EDS}}$$

As both are known in the reference sample one can determine the value of $\frac{cal_{Pb}}{cal_{Br}}$ which can then be used and multiplied by $\frac{Pb_{EDS}}{Br_{EDS}}$ of the sample of interest to determine $\frac{Pb_{real}}{Br_{real}}$.

In our case, we were not interested in the Pb/Br ratio in the material, but in the variation of this ratio between the bleached and not-bleached zones. This can be easily determined without performing any calibration since the calibration factors cancel when taking the ratio as in (r)

$$\text{(r)}\ \frac{\frac{Pb^{Bleach}_{real}}{Br^{Bleach}_{real}}}{\frac{Pb^{Ref}_{real}}{Br^{Ref}_{real}}} = \frac{\frac{cal_{Pb}}{cal_{Br}} * \frac{Pb^{Bleach}_{EDS}}{Br^{Bleach}_{EDS}}}{\frac{cal_{Pb}}{cal_{Br}} * \frac{Pb^{Ref}_{EDS}}{Br^{Ref}_{EDS}}} = \frac{\frac{Pb^{Bleach}_{EDS}}{Br^{Bleach}_{EDS}}}{\frac{Pb^{Ref}_{EDS}}{Br^{REf}_{EDS}}}$$

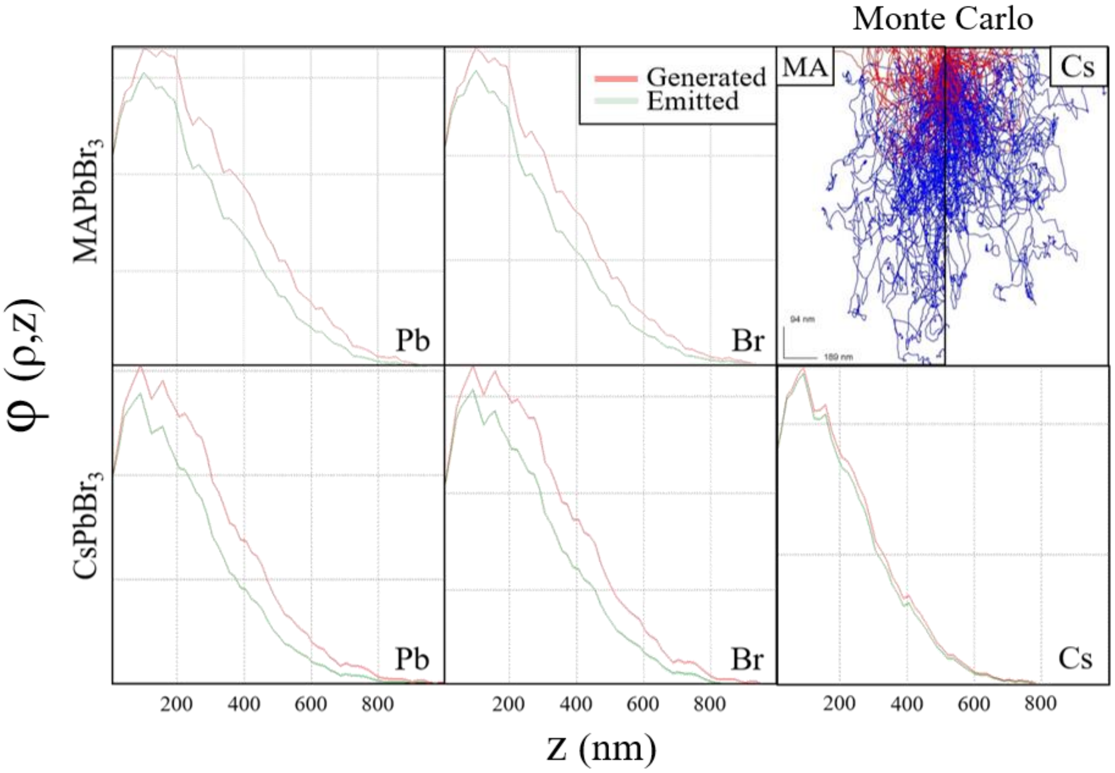

Figure.S8 :.Phi-Rho-Z (φρz) curves for $MaPbBr_3$ (first line) and $CsPbBr_3$ (second line) as function of z, the depth inside the crystal. Since not all the generated X-rays are emitted from the surface we report two curves. The red curve corresponds to the amount of generated X-rays in function of z. The green curve is the amount of the X-rays effectively able to exit the surface in function of z. Curves for LEFT: Pb; MIDDLE: Br; RIGHT: Cs. In the upper right corner, we show graphically the simulation of the e-beam scattering into the $MaPbBr_3$ (left) and $CsPbBr_3$ (right).

In the main text we referred to the fact that the EDS penetration depths actually create artifacts in evaluating the variation of the composition on the surface, because some signal comes from deeper layers. We evaluated this issue with the software Win X-Ray 1.4.2[19] for the incident voltage of 10 kV. As can be seen in Figure S7, the peak of the signal comes from around 150 nm. If we integrate the signal coming from the first 50 nm, we see that it corresponds to approximately 1/10 of the total integral. Figure S7 shows the results of the calculated Phi-Rho-Z (φ ρ z) curves for $MaPbBr_3$ (first line) and $CsPbBr_3$ (second line) as function of z, the depth inside the crystal. The value on the y axis, namely phi (φ), corresponds to the electron beam-induced ionization distribution in the material. In red is reported the origin and amount of the generated X-rays in the material. In green is the origin and amount of the X-rays effectively able to be emitted by the material, because part of them is reabsorbed. The amount of generated and emitted X-rays depends on the density of the material rho (ρ)(MA 3.83 $g\bullet cm^{-3}$, Cs 5.4 $g\bullet cm^{-3}$) and from the depth (z).

SI.14. XPS measurements.

XPS measurements were carried out with Kratos AXIS ULTRA system using a monochromatic Al Kα X-ray source (hν = 1486.6 eV) at 75W and detection pass energies ranging between 20 and 80 eV. Curve fitting analysis was based on linear or Shirley background subtraction and application of Gaussian-Lorenzian line shapes.

SI.15. Bibliography

1 D. R. Ceratti, Y. Rakita, L. Cremonesi, R. Tenne, V. Kalchenko, M. Elbaum, D. Oron, M. A. C. Potenza, G. Hodes and D. Cahen, *Advanced Materials*, 2018, **30**, 1706273.
2 B. Wenger, P. K. Nayak, X. Wen, S. V. Kesava, N. K. Noel and H. J. Snaith, *Nature Communications*, 2017, **8**, 590.
3 Q. Dong, Y. Fang, Y. Shao, P. Mulligan, J. Qiu, L. Cao and J. Huang, *Science*, 2015, **347**, 967–970.
4 D. Shi, V. Adinolfi, R. Comin, M. Yuan, E. Alarousu, A. Buin, Y. Chen, S. Hoogland, A. Rothenberger, K. Katsiev, Y. Losovyj, X. Zhang, P. A. Dowben, O. F. Mohammed, E. H. Sargent and O. M. Bakr, *Science*, 2015, **347**, 519–522.
5 N. Onoda-Yamamuro, T. Matsuo and H. Suga, *Journal of Physics and Chemistry of Solids*, 1990, **51**, 1383–1395.
6 D. Weber, *Zeitschrift für Naturforschung B,* 2014, **33**, 1443–1445.
7 R. Heiderhoff, T. Haeger, N. Pourdavoud, T. Hu, M. Al-Khafaji, A. Mayer, Y. Chen, H.-C. Scheer and T. Riedl, *J. Phys. Chem. C*, 2017, **121**, 28306–28311.
8 null Perdew, null Burke and null Ernzerhof, *Phys. Rev. Lett.*, 1996, **77**, 3865–3868.
9 A. Tkatchenko and M. Scheffler, *Phys. Rev. Lett.*, 2009, **102**, 073005.
10 G. Kresse and J. Furthmüller, *Phys. Rev. B*, 1996, **54**, 11169–11186.
11 G. Kresse and D. Joubert, *Phys. Rev. B*, 1999, **59**, 1758–1775.
12 G. A. Elbaz, D. B. Straus, O. E. Semonin, T. D. Hull, D. W. Paley, P. Kim, J. S. Owen, C. R. Kagan and X. Roy, *Nano Lett.*, 2017, **17**, 1727–1732.
13 C. C. Stoumpos, C. D. Malliakas, J. A. Peters, Z. Liu, M. Sebastian, J. Im, T. C. Chasapis, A. C. Wibowo, D. Y. Chung, A. J. Freeman, B. W. Wessels and M. G. Kanatzidis, *Crystal Growth & Design*, 2013, **13**, 2722–2727.
14 S. R. Raga, Y. Jiang, L. K. Ono and Y. Qi, *Energy Technology*, 2017, **5**, 1750–1761.
15 F. C. Schaefer, I. Hechenbleikner, G. A. Peters and V. P. Wystrach, *J. Am. Chem. Soc.*, 1959, **81**, 1466–1470.
16 C. C. Stoumpos, C. D. Malliakas and M. G. Kanatzidis, *Inorg. Chem.*, 2013, **52**, 9019–9038.
17 290-87-9 CAS MSDS (1,3,5-Triazine) Melting Point Boiling Point Density CAS Chemical Properties, https://www.chemicalbook.com/ChemicalProductProperty_US_CB9203224.aspx, (accessed May 11, 2019).
18 Y. Zhou, M. Yang, S. Pang, K. Zhu and N. P. Padture, *J. Am. Chem. Soc.*, 2016, **138**, 5535–5538.
19 R. Gauvin, E. Lifshin, H. Demers, P. Horny and H. Campbell, *Microscopy and Microanalysis*, 2006, **12**, 49–64.